QUANTITATIVE CALCULATION OF ACQUISITION FOOTPRINTS FOR 3D LAND SEISMIC ACQUISITION GEOMETRIES

WEI WEI, WEIJIA SUN and LI-YUN FU

Key Laboratory of Petroleum Resources, Institute of Geology and Geophysics, Chinese Academy of Sciences, Beijing 100029, P.R. China. caswei@gmail.com

(Received February 27, 2014; revised version accepted December 10, 2014)

ABSTRACT

Wei, W., Sun, W. and Fu, L.-Y., 2015. Quantitative calculation of acquisition footprints for 3D land seismic acquisition geometries. *Journal of Seismic Exploration*, 24: 83-102.

An inappropriate acquisition geometry can leave a strong footprint on the stack of 3D seismic data, which would reduce the accuracy of seismic processing and interpretation. However, it is difficult to completely eliminate acquisition footprints using processing methods. In this paper, we propose a quantitative method to calculate the acquisition footprints for given 3D land seismic acquisition geometries, which improves on the usually qualitative methods used in classical seismic geometry design. Our method can obtain the acquisition footprints at any target depth based on the seismic wave propagation (WRW) model in terms of matrix operators in the frequency domain. The footprint is expressed as relative amplitudes of a stacked image of primaries for every source-receiver pair. With the proposed approach, we could quantitatively evaluate the acquisition footprints of different seismic acquisition schemes for any target depth and ultimately choose the optimal acquisition parameters that would yield the minimal possible footprint before initiating fieldwork. Through two theoretical examples, we investigate the influence two key acquisition parameters, the shot traverse spacing DS and the number of receiver lines repeated in a crossline roll-along K, have on acquisition footprints. Herein, a case study in an oilfield in China is presented by computing the footprint at different depths for different acquisition geometries. The results show that the qualities of the seismic migrations can be greatly improved by choosing the optimal geometry, which has the smallest possible acquisition footprint.

KEY WORDS: acquisition footprints, seismic survey design, seismic geometry, target-depth-dependent, seismic wave propagation.

0963-0651/15/$5.00

INTRODUCTION

Ideally, the seismic amplitude would be the same for each subsurface bin from one survey to the next, but in reality, the amplitude for each bin varies from survey to survey, which is usually the result of seismic acquisition geometry. This phenomenon is commonly known as an acquisition footprint. One primary cause of acquisition footprints is the practical application of seismic acquisition schemes that are not full-fold (Marschall, 1999). In a paper by Marschall (1999), it was proved that only a full-fold scheme can avoid acquisition footprints.

Cordsen (2004) determined that two main contributions to acquisition footprints are geometry effects (e.g., fold variations, source and receiver line spacing and orientations, wide or narrow patch geometry, source-generated noise) and non-geometry effects (e.g., topography, culture, weather, surface conditions). Acquisition footprint occurrence is highly correlated with the geometric distribution of sources and receivers at the earth's surface (Marfurt et al., 1998). Surface geometry often leaves a regular amplitude and phase imprint on the stack of 3D seismic data. In this study, we discuss the geometry effects resulting from dissimilarities between adjacent common mid-point (CMP) bins. Acquisition footprints can easily be induced in seismic data processing by any 3D seismic survey. Mild or strong acquisition footprints may obscure the true reflection responses of the subsurface and further reduce the accuracy of seismic processing and interpretation (Canning and Gardner, 1998; Gesbert, 2002; Al-Bannagi et al., 2005; Brown, 2010). Therefore, acquisition footprints should be taken into account in seismic acquisition. Essentially, acquisition footprints result from sacrificing 3D folds for economic reasons, causing the appearance of local resampling aliasing (Marschall, 1997, 2003).

Fold variations are the simplest form of acquisition footprints (Cordsen, 2004). Because fold changes with offset, each offset range has different fold contributions. Since each individual bin of a 3D survey has differing offset distributions, the CMP stack of all traces in a bin shows amplitude variations from bin to bin, which produces an acquisition footprint. Based on this important fact, Hill et al. (1999) found that limited-offset fold-of-stack plots, especially near-offset fold-of-stack plots, are effective in the qualitative analysis of the effect of acquisition footprints. Schuster and Liu (2001) reported that the seismic array theorem is a practical tool to analyze acquisition footprints after seismic migration for homogeneous media. Focal beam analysis (Berkhout et al., 2001; Volker et al., 2001; Van Veldhuizen et al., 2008; Wei et al., 2012) can also be used to perform footprint analysis. Symmetric acquisition geometries (Vermeer, 1998) with identical sampling of shots and receivers can preserve the spatial continuity of seismic wavefields, which is beneficial in decreasing the acquisition footprint. Vermeer (1997, 2012) and Savage and Mathewson (2001) predicted 3D seismic footprints from existing 2D/3D data and evaluated 3D

survey designs before acquisition. Cooper et al. (2008) examined acquisition footprints in a seismic synthetic dataset by numerical modeling. Di et al. (2008) employed physical modeling to obtain the footprints of wide/narrow azimuth acquisition and show their effects on seismic imaging. However, most of these methods are qualitative or time-consuming in their attempts to eliminate acquisition footprints in seismic geometry designing. Thus, a rapid and quantitative method that can intuitively yield acquisition footprints in a way similar to traditional fold analysis is necessary. This phenomenon has been noticed for many years, but little progress has been made.

Acquisition footprints are non-uniform amplitude distributions among bins caused by different offset and azimuth distributions among the bins of a 3D survey. Physically, footprints can be considered as an amplitude-weighted linear summation of every limited-offset fold of stack. In this paper, we propose a quantitative acquisition footprint analysis for homogeneous media. The proposed method calculates the relative amplitudes of CMP stacks or migrations in individual bins at any target depth and yields acquisition footprints in a manner similar to traditional fold analysis. With the relative amplitudes of all the bins, we can analyze the footprint distribution at any target depth for a given acquisition geometry. This footprint analysis method can be a practical tool in designing 3D seismic surveys by borrowing the idea of a rapid trial-and-error method. The best survey may be the one with the weakest acquisition footprint.

Finally, a case study for 3D seismic acquisition in an oilfield of China is carried out. The two acquisition geometries with different footprint distributions are evaluated through both the proposed theoretical computation and seismic migration at different target depths. The seismic data acquired by these acquisition schemes are processed using the same processing flow and processing parameters for convenience in comparison. The resulting seismic images qualitatively agree with the prior theoretical analysis of acquisition footprint distributions for these acquisition geometries.

THEORETICAL CALCULATION METHOD OF ACQUISITION FOOTPRINTS

An acquisition footprint is physically defined as an amplitude-weighted linear summation of every limited-offset fold of stack. In this section, we will derive the calculation of an acquisition footprint. We first derive formulae to calculate the amplitude weight for different source-receiver pairs in a single bin. Then, a quantitative footprint is obtained by summing the amplitude weights of the source-receiver pairs for each individual bin.

For convenience, we assume that a point source harmonically oscillates with an angular frequency of w for each shot. In a 3D homogeneous medium,

the propagation of a seismic wavefield with wavenumber k is described by the propagation operator

$$W(\mathbf{r}_r,\mathbf{r}_s) = W(\mathbf{r}_r)W(\mathbf{r}_s) \quad . \tag{1}$$

Eq. (1) is the multiplication of the receiver propagation operator $W(\mathbf{r}_r)$ with the source propagation operator $W(\mathbf{r}_s)$ at a target depth z_t, which can be expressed as (Berkhout, 1982)

$$W(\mathbf{r}_r) = (1/2\pi)[(1 + jk\Delta r_r)/\Delta r_r]\cos\theta_r(e^{-jk\Delta r_r}/\Delta r_r) \quad , \tag{2}$$

$$W(\mathbf{r}_s) = (1/2\pi)[(1 + jk\Delta r_s)/\Delta r_s]\cos\theta_s(e^{-jk\Delta r_s}/\Delta r_s) \quad . \tag{3}$$

The operators in eqs. (1), (2) and (3) have the following meaning (Fig. 1):

- $\mathbf{r}_r(\Delta x_r,\Delta y_r,\Delta z_r)$ is the displacement vector from the target point $T(\Delta x_t,\Delta y_t,\Delta z_t)$ to the receiver point $R(\Delta x_r,\Delta y_r,\Delta z_r)$ with $\Delta x_r = x_r - x_t$, $\Delta y_r = y_r - y_t$, and $\Delta z_r = z_r - z_t$.

- $\mathbf{r}_s(\Delta x_s,\Delta y_s,\Delta z_s)$ is the displacement vector from the shot point $S(\Delta x_s,\Delta y_s,\Delta z_s)$ to the target point $T(\Delta x_t,\Delta y_t,\Delta z_t)$ with $\Delta x_s = x_t - x_s$, $\Delta y_s = y_t - y_s$, and $\Delta z_s = z_t - z_s$.

- $\Delta r_r = \sqrt{\{(x_r-x_t)^2 + (y_r-y_t)^2 + (z_r-z_t)^2\}}$ is the length of the displacement vector $\mathbf{r}_r(\Delta x_r,\Delta y_r,\Delta z_r)$.

- $\Delta r_s = \sqrt{\{(x_s-x_t)^2 + (y_s-y_t)^2 + (z_s-z_t)^2\}}$ is the length of the displacement vector $\mathbf{r}_s(\Delta x_s,\Delta y_s,\Delta z_s)$.

- $\cos\theta_r = (z_t - z_r)/\Delta r_r$ is the cosine of a reflection angle for the target point.

- $\cos\theta_s = (z_t - z_s)/\Delta r_s$ is the cosine of an incident angle for the target point.

Under the far-field approximation, eqs. (2) and (3) can be rewritten as

$$W(\mathbf{r}_r) = (jk/2\pi)\cos\theta_r(e^{-jk\Delta r_r}/\Delta r_r) \quad , \tag{4}$$

and

$$W(\mathbf{r}_s) = (jk/2\pi)\cos\theta_s(e^{-jk\Delta r_s}/\Delta r_s) \quad . \tag{5}$$

Eq. (1) can be used to represent the seismic stacked operator of a point scatter at target depth z_t. From the common focus point approach (Berkhout, 1982; 1997), the seismic migrated operator of a point scatter corresponds to double focusing the seismic stacked operator $W(\mathbf{r}_r, \mathbf{r}_s)$ in accordance with

$$P(\mathbf{r}_r,\mathbf{r}_s) = F(\mathbf{r}_r)W(\mathbf{r}_r)W(\mathbf{r}_s)F(\mathbf{r}_s) \quad , \tag{6}$$

where $F(\mathbf{r}_r)$ is the receiver focusing operator and $F(\mathbf{r}_s)$ is the source focusing operator. Combining the migrated operator $P(\mathbf{r}_r,\mathbf{r}_s)$ and the reflection operator R(p), may result in the amplitude weight of the migrated image for every source-receiver pair. Since focusing is the reverse process of wave propagation, the focusing operators $F(\mathbf{r}_r)$ and $F(\mathbf{r}_s)$ are approximately equal to the conjugate complex of the propagation operators $W(\mathbf{r}_r)$ and $W(\mathbf{r}_s)$, respectively (Berkhout, 1987). Correspondingly, the acquisition footprints of a migrated image can be simplified to the case of a stacked image. Note that, in the processing of migration, the focusing operators $F(\mathbf{r}_r)$ and $F(\mathbf{r}_s)$ may include terms for correcting the footprint of the acquisition geometry. Let us for a moment assume that such corrections are not implemented, such that the footprint of the acquisition geometry becomes clear in our analysis.

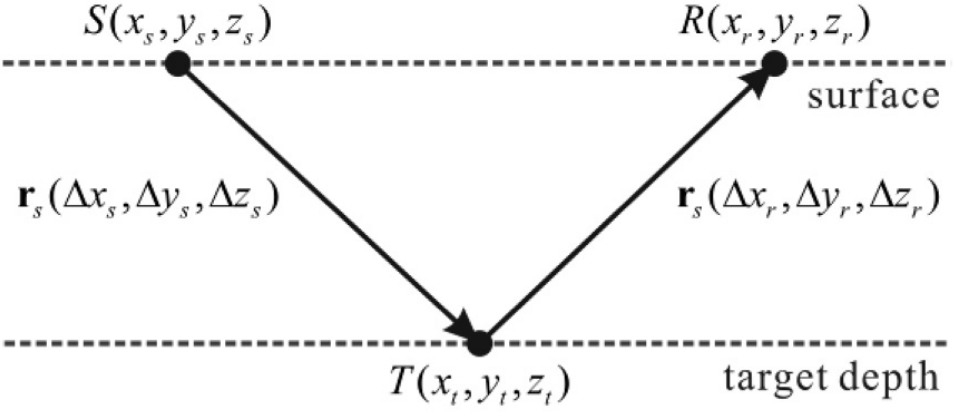

Fig. 1. Schematic diagram of wave propagation. Wave propagates form the source $S(x_s,y_s,z_s)$ at the surface to the target $T(x_t,y_t,z_t)$ at a target depth of z_t and reflected to the detector $R(x_r,y_r,z_r)$ at the surface. The arrows in the figure indicate the directions of wave propagations.

Consider a planar interface through the scatter point separating two acoustic media with P-wave velocities α_1 and α_2 and densities ρ_1 and ρ_2 (Fig. 2). A plane P-wave incident on the interface at angle θ_1 generates a reflected P-wave with a reflection angle of θ_1 ($\theta_1 = \theta_r = \theta_s$ for a horizontal layer) and a transmitted P-wave with a transmission angle of θ_2. It is known that, for a plane interface, the Zoeppritz equations give the P-wave reflection and transmission coefficients as functions of six independent elastic parameters and the angles of incidence. Mallick (1993) derived an approximate formula describing the Zoeppritz equations for the plane P-wave reflection coefficient as a function of the ray parameter given by

$$R(p) \approx R_f(p) = (\rho_2 q_{\alpha 1} - \rho_1 q_{\alpha 2})/(\rho_2 q_{\alpha 1} + \rho_1 q_{\alpha 2}) \quad , \tag{7}$$

where $R_f(p)$ is the 'fluid-fluid' reflection coefficient, i.e., the reflection coefficient between the two adjacent layers when the shear speeds are set to zero in both media (Officer, 1958). The ray parameter p is the horizontal slowness that is preserved in the primary and mode converted waves through Snell's law

$$p = \sin\theta_1/\alpha_1 = \sin\theta_2/\alpha_2 \quad , \tag{8}$$

and the quantities $q_{\alpha 1}$ and $q_{\alpha 2}$ are the vertical slownesses of the respective waves in their media

$$q_{\alpha 1} = \cos\gamma_1 /\alpha_1 \quad , \tag{9}$$

$$q_{\alpha 2} = \cos\gamma_2 /\alpha_2 \quad . \tag{10}$$

Substituting eqs. (8), (9) and (10) into eq. (7), the reflection operator can be simplified as

$$R(p) = [\rho_2\alpha_2\cos(\alpha_1) - \rho_1\alpha_1\cos(\alpha_2)]/[\rho_2\alpha_2\cos(\alpha_1) + \rho_1\alpha_1\cos(\alpha_2)] \quad . \tag{11}$$

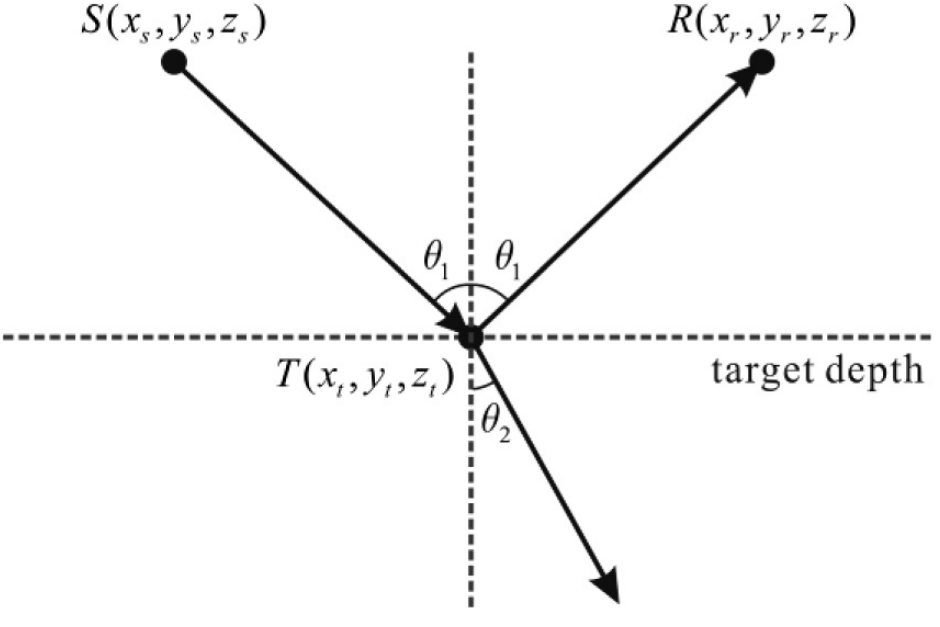

Fig. 2. A plane P-wave reflection and transmission between two layers at a planar interface with a target depth of z_t. Upper medium has a P-wave velocity α_1 and density ρ_1. Lower medium has a P-wave velocity α_2 and density ρ_2. A plane P-wave incident on the interface at an angle θ_1 generates a plane P-wave with angles of reflection θ_1 and a plane P-wave with angles of transmission θ_2, respectively. The arrows in the figure indicate the directions of wave propagations.

Combining the stacked operator $W(\mathbf{r}_r,\mathbf{r}_s)$ from eqs. (4) and (5) and the reflection operator R(p) from eq. (11), we obtain the amplitude weight C of the stacked image for every source-receiver pair as

$$C = |WRW| = [k^2\cos(\alpha_1)/4\pi^2 r]$$

$$\times [\rho_2\alpha_2\cos(\alpha_1) - \rho_1\alpha_1\cos(\alpha_2)]/[\rho_2\alpha_2\cos(\alpha_1) + \rho_1\alpha_1\cos(\alpha_2)] \quad . \qquad (12)$$

The weight C in eq. (12) is actually the relative amplitude of the CMP stack in each individual bin, which is different from conventional CMP stacks. In other words, the weight C in the conventional fold calculation is equal to 1 for every source-receiver pair. Obviously, the weight C in eq. (12) makes the footprint analysis quantitative and accurate. After iteratively calculating the relative amplitudes of every bin, we can produce the footprint distribution for the whole 3D acquisition geometry at target depth z_t. This proposed acquisition footprint analysis would be a practical tool to design 3D seismic surveys by a rapid trial-and-error method, where the best survey might be the one with the weakest acquisition footprint.

Note that eq. (12) considers only the stack response of the primary reflections. Although it would be better during acquisition design to consider noises, such as multiples and ground roll, they are neglected. This is appropriate, because these noises can be largely suppressed by seismic processing procedures.

THEORETICAL EXAMPLES

Using inappropriate acquisition parameters can lead to severe seismic acquisition footprints. Of all acquisition parameters, the parameters of inline/crossline rolling distance have the most significant influence on the calculation of acquisition footprints shown in the previous section. For convenience, we use the same symbols as Marschall (1999, 2003), given in Table 1. Marschall (1999, 2003) defined the reference acquisition geometry, i.e., the full-fold geometry, as $\Delta G = \Delta S = \Delta g = \Delta s$. This case yields no footprint and has the smallest possible number of different bin configurations (BSC number), which is 2. The BSC number, proposed by Marschall (1997), is a key quantity to evaluate the degree of homogeneity for a given acquisition geometry in terms of the signal-to-noise (S/N) ratio. Ideal geometries have as small a BSC number as possible. Here, we use the full-fold geometry as a reference in the followed comparisons.

Effect of shot traverse spacing ΔS

The shot traverse spacing, listed in Table 1 as ΔS, is also known as the inline rolling distance. In this section, we calculate the acquisition footprint values for three seismic 3D land acquisition geometries with different ΔS values. Three land acquisition schemes with different ΔS values, named Schemes I, II, and III, are compared. All three schemes use the same geometry template, which is shown in Fig. 3. For the template, we have $X = 8$, $N_S = 4$, $N_G = 64$, $a = \Delta g = \Delta s = 100$ m, and $\Delta G = 400$ m. In the three schemes, the crossline coverage C_y remains at a constant maximum value, that is, $K = X - 1 = 7$, which gives a homogeneous scheme along the crossline direction. For Schemes I, II, and III, ΔS = 200, 400, and 800 m, respectively. Thus, we have $C_y = X/2 = 4$, and $C_x = (N_G/2) * (\Delta g/\Delta S) = 16$, 8, and 4 for Schemes I, II, and III, respectively. Then, the total fold $C_{3D} = C_x * C_y$ is given as 64, 32, and 16 for Schemes I, II, and III, respectively. Correspondingly, the BSC numbers are 16, 32, and 64, respectively.

Table 1. Symbols of acquisition parameters given by Marschall (1999, 2003).

Symbol	Description
a	side length of square bin at surface
Δx, Δy	side length of bin in subsurface, where usually one has: $\Delta x = \Delta y = a/2$
X	number of active receiver lines
ΔG	spacing between adjacent receiver lines
ΔS	spacing of shot traverse or inline rolling distance
Δg	channel spacing on individual receiver line or station interval
Δs	shot interval
N_G	number of active channels per receiver line
N_S	number of shotpoints per shot traverse
C_x	inline coverage: $C_x = (N_G/2) * (\Delta g/\Delta S)$
C_y	crossline coverage, where usually we have the relationship: $C_y = X/2$
C_{3D}	total coverage, where $C_{3D} = C_x * C_y$
K	number of receiver lines to be repeated in crossline roll-along
BSC	smallest actual number of different bin configurations

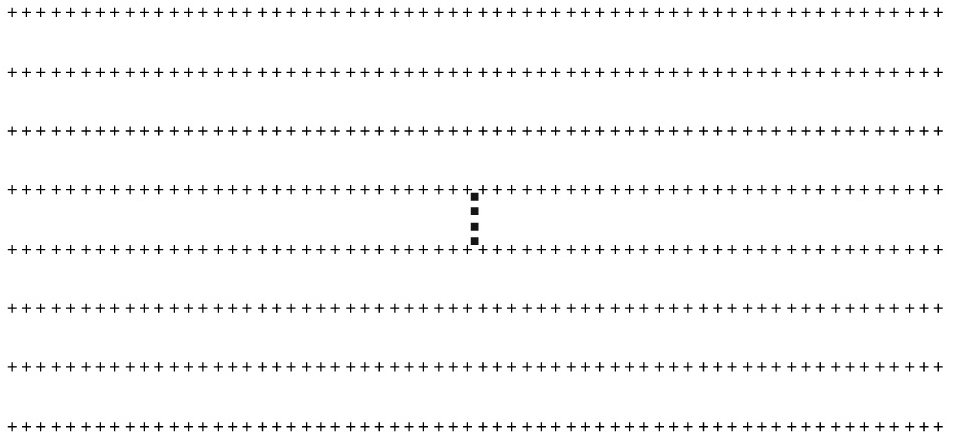

Fig. 3. The geometry template for three orthogonal acquisition Schemes I, II, and III, in which the solid square ■ represents sources and the cross + indicates detectors. The template consists of 8 detector lines, each 6400 m in length, with 400-m spacing between the lines and a 100-m detector interval.

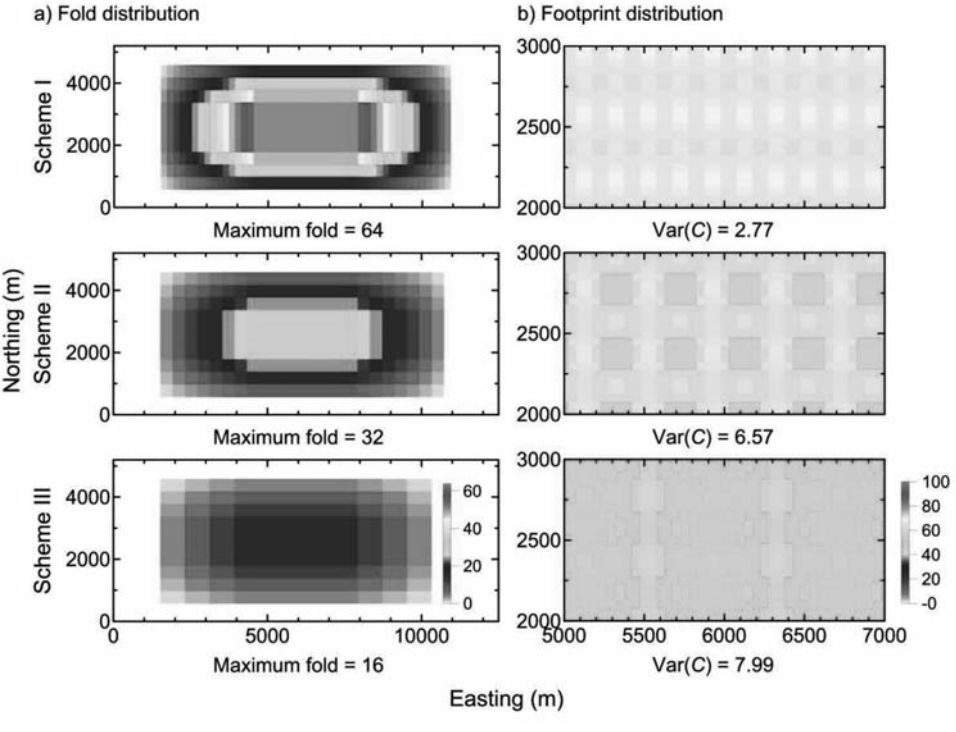

Fig. 4. Distributions of fold (a) and footprint (b) for acquisition Schemes I, II, and III, respectively.

The distributions of the fold of stack and the footprints are shown in Fig.s 4a and 4b, respectively. The footprint at a depth of 1500 m is calculated using eq. (12). The grey scales at each point in the subgraphs indicates the relative amplitude for a CMP bin. In Fig. 4b, some striping is observed along the inline direction (east to west) across the entirety of the distributions; the striping varies between acquisition schemes and presents an uneven distribution. Schemes II and III show much heavier striping effects (footprints) than Scheme I, because they employ a larger inline sampling than that of Scheme I. To further investigate the footprints, we compute the variance of the footprint maps in Fig. 4b within the full-fold area. The variance Var(C) = 2.77, 6.57, and 7.99 for Schemes I, II, and III, respectively. The variance demonstrates that Scheme I shows a more uniform footprint distribution than Schemes II and III. This is because Scheme I has the smallest inline rolling distance ΔS and the highest fold C_{3D}. Actually, the total fold C_{3D} is inversely proportional to the inline rolling distance ΔS. In conclusion, as ΔS increases, the inline acquisition continuity decreases rapidly, as expected. That means that the larger the ΔS, the heavier the resulting footprint, and vice versa.

Effect of the number of receiver lines repeated in crossline roll-along K

Generally, K, the number of receiver lines to be repeated in the crossline roll-along, is explained as the crossline rolling distance ΔD. These two variables have a simple relationship, $\Delta D = (X - K) * \Delta G$. In this section, we calculate the acquisition footprint values for three seismic land acquisition geometries with different K values. Three land acquisition schemes with different K values, named Schemes IV, V, VI are compared. Fig. 5 shows the geometry templates for Schemes IV, V, and VI. For the template, we have X = 8, NG = 64, $a = \Delta g = \Delta s$ = 100 m, $\Delta G = \Delta S$ = 400 m, and NS = 4, 8, and 16 for Schemes IV, V, and VI, respectively. Then the inline coverage C_x = 8, and the crossline coverage $C_y = X/2 = 4$. Finally, the total coverage C_{3D} is 32 for all three schemes. Correspondingly, the BSC numbers are 32, 64, and 128, respectively. The acquisition parameters for the three schemes are listed in Table 2.

The folds and footprints of Schemes IV, V, and VI, are shown in Figs. 6a and 6b, respectively. The footprints are calculated from eq. (12) at a depth of 1500 m. The grey scales at each point in the subgraphs indicates the relative amplitude for a CMP bin. In Fig. 6b, some striping is observed along the crossline direction (north to south) across the entirety of the distributions; the striping varies between acquisition schemes and presents an uneven distribution. Scheme VI shows much heavier striping effects (footprints) than Schemes IV and V, because it employs a larger crossline sampling. To further investigate the footprint distribution, we compute the variance of the footprint maps in Fig. 6b within the full-fold area. The variance Var(C) = 6.57, 6.60, and 11.43 for Schemes IV, V, and VI, respectively.

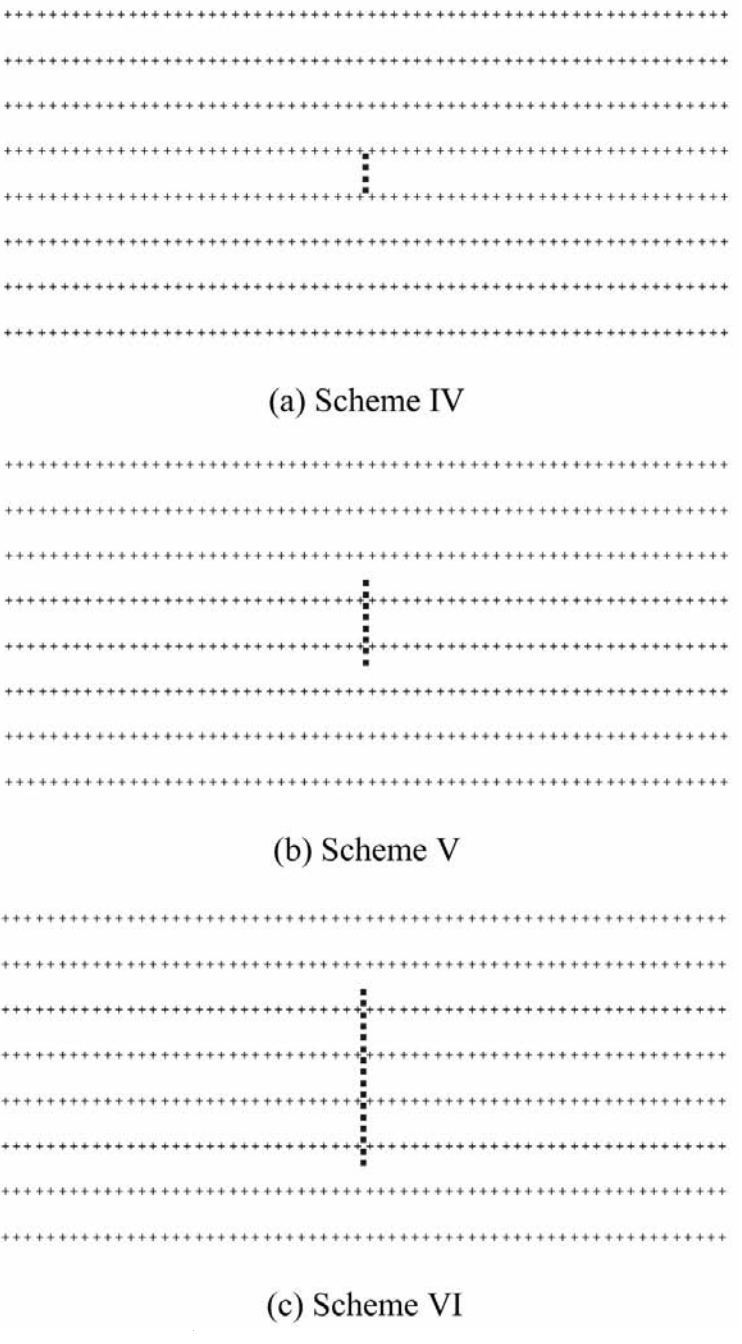

Fig. 5. The geometry templates for three orthogonal acquisition Schemes IV (a), V (b), and VI (c). The square ■ represents sources and the cross + indicates detectors. All templates consist of 8 detector lines, each 6400 m in length with 400-m spacing between the receiver lines and a 100-m detector interval. The source number are 4, 8, and 16, respectively, with a 400-m spacing transversely. The detailed acquisition parameters are given in Table 1.

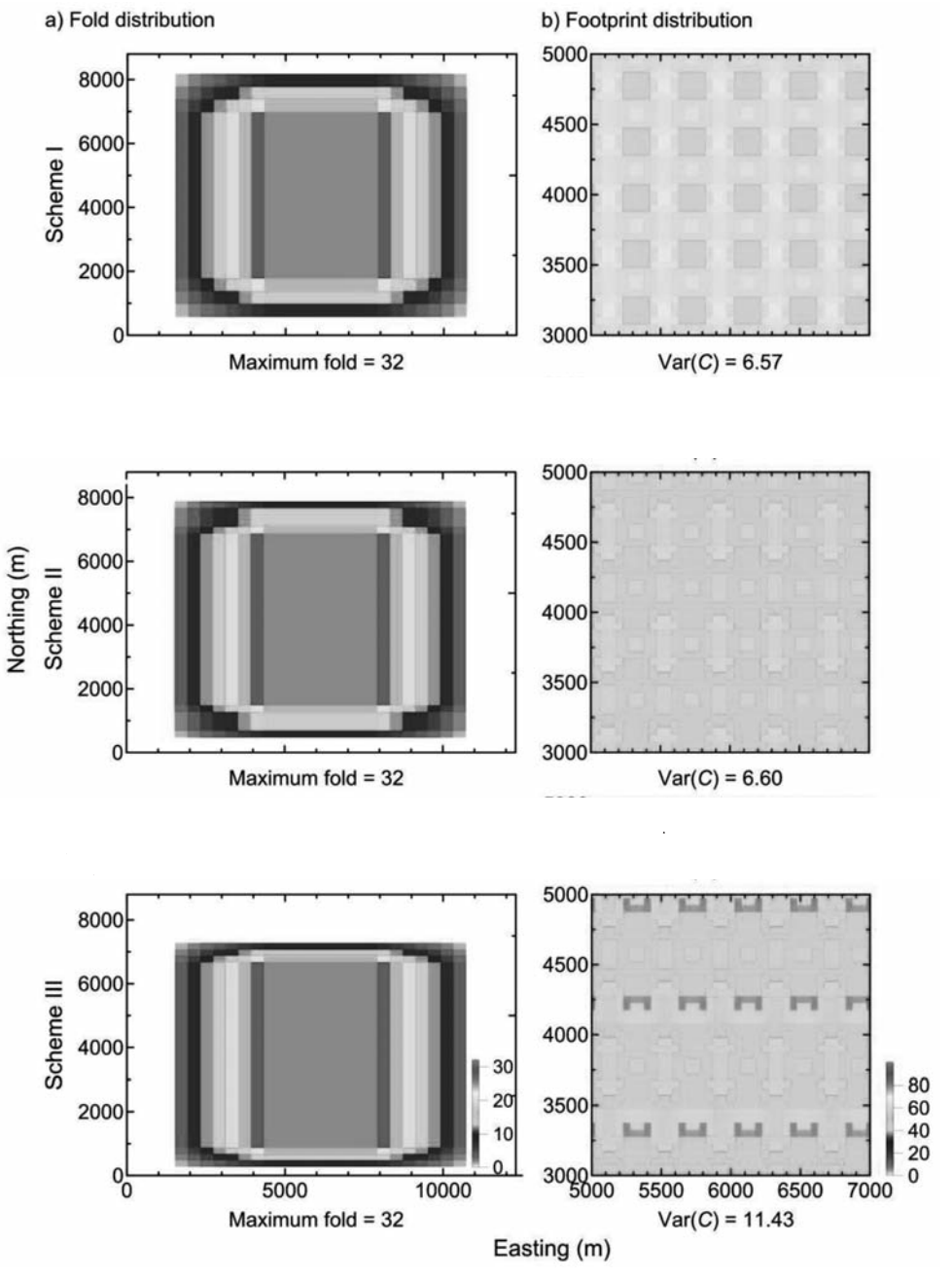

Fig. 6. Distributions of fold (a) and footprint (b) for acquisition Schemes IV, V and VI (see Table 2), respectively.

Table 2. Parameters of three acquisition geometries (Scheme IV, V and VI).

Survey	Geometry	Detector point distance	Source point distance	Detector line distance	Source line distance	Bin size		Folds	In-line rolling distance	Cross-line rolling distance
Scheme IV	8L4S64R	100m	100m	400m	400m	25m	50m	32	400m	400m
Scheme V	8L8S64R	100m	100m	400m	400m	50m	50m	32	400m	800m
Scheme VI	8L16S64R	100m	100m	400m	400m	50m	50m	32	400m	1600m

The variance demonstrates that Schemes IV and V show a more uniform footprint distribution than Scheme VI. Although Schemes IV and V show similar variance values, Scheme IV shows a slightly better distribution than Scheme V. In conclusion, as K decreases, the crossline acquisition continuity decreases, as expected. That means that the smaller K is, the heavier the footprint is, and vice versa.

In the case of Schemes IV, V, and VI, one problem should be noted: the maximum offsets for the three schemes are different. The maximum inline offset is given as 3150 m for all three schemes, while the maximum crossline offsets are given as 1550, 1750, and 2150 m, respectively. The resulting maximum offsets for the three schemes are given as 3511, 3604, and 3814 m, respectively. Scheme IV has the smallest maximum offset of the three schemes. That means that Schemes V and VI have much larger offsets (i.e., offsets larger than 3511 m) that contribute more to the total 3D coverage than Scheme IV. In other words, if the contributions of offsets greater than 3511 m for Schemes V and VI are muted, the total 3D coverage would be smaller than 32. Correspondingly, the footprints of Schemes V and VI will be more severe than those shown in Fig. 6b.

CASE STUDIES

Applications of the acquisition footprint analysis for different acquisition geometries are conducted in oilfield of China. We took two orthogonal acquisition templates as examples. For the template, we have $X = 32$, $N_S = 8$, $N_G = 128$, $\Delta g = 50$ m, $\Delta s = 100$ m, $\Delta G = 50$ m, $\Delta S = 100$ and 400 m for Schemes VII and VIII, respectively. Then the inline coverage C_x equals 32 and 8 for Schemes VII and VIII, respectively, while the crossline coverage C_y equals

X/4 = 8 for both schemes due to the crossline rolling distance of 800 m. Finally, the total coverage values C_{3D} are 256 and 64 for Schemes VII and VIII shown in Figs. 8a and 8b, respectively. The detailed acquisition parameters are listed in Table 3. Scheme VII is the acquisition geometry that was originally implemented in the field. Scheme VIII is a one-quarter version of the source density simplified from Scheme VII. The number of receiver lines repeated in crossline roll-along are the same, K = 16, which corresponds to inhomogeneous implementation. The difference between Schemes VII and VIII is that the shot traverse spacings ΔS equal 100 and 400 m, respectively.

Table 3. Parameters of three acquisition geometries (Scheme VII and VIII).

Survey	Geometry	Detector point distance	Source point distance	Detector line distance	Source line distance	Bin size		Folds	In-line rolling distance	Cross-line rolling distance
Scheme VII	32L8S128R	50m	100m	50m	100m	25m	25m	256	100m	800m
Scheme VIII	32L8S128R	50m	100m	50m	400m	25m	25m	64	400m	800m

The evaluations of the acquisition footprints for Schemes VII and VIII (see Fig. 7) are performed at different depths from 500 to 2000 m with an interval of 500 m. The footprint maps for Schemes VII and VIII at different depths are shown in Fig. 9. Comparing Fig. 9a with Fig. 9b, the footprints of Scheme VII are much better than those of Scheme VIII at all depths ranging

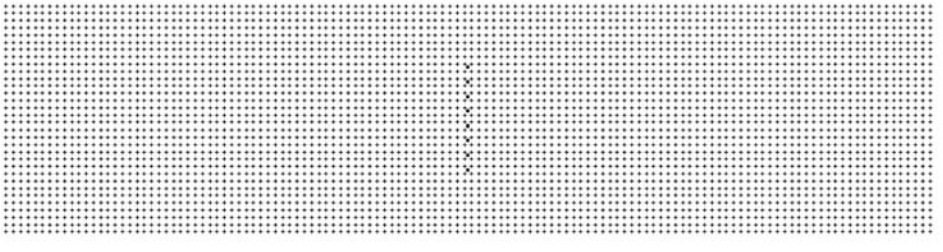

Fig. 7. The template for two orthogonal acquisition geometries (Scheme VII and VIII), consisting of 32 detector lines. The length of receiver line is 6400 m. The square ■ represents sources and the cross + indicates detectors. The detailed acquisition parameters are given in Table 3.

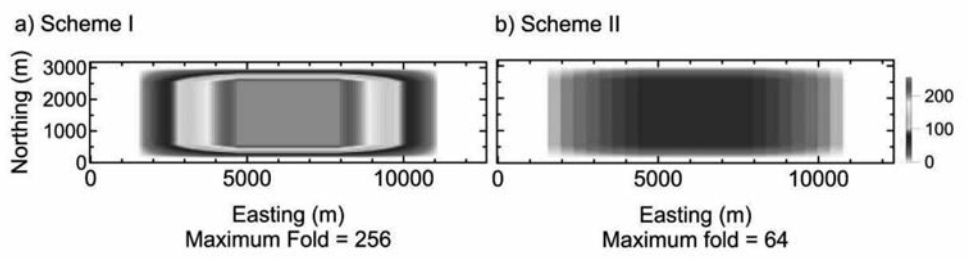

Fig. 8. Fold distributions for acquisition Scheme VII (a) and VIII (b) (Table 3).

from 500 m to 2000 m. Another phenomenon is that the footprint effect becomes weaker as the depth increases for both schemes. The footprints at a depth of 2000 m are almost invisible, while the footprints at a depth of 500 m are quite clear. We have BSC = 32 for Scheme VII and BSC = 256 for Scheme VIII. Recalling that the minimum BSC value is 2, corresponding to the full-fold scheme, these BSC values mean that the smaller the BSC, the better the acquisition geometry. Although it is not ideal, Scheme VII is much better than Scheme VIII when considering the BSC.

A 3D seismic acquisition based on Scheme VII was carried out in an oilfield in China in 2007. To compare the footprints of the two schemes, we extracted seismic data according to acquisition Scheme VIII. To avoid the influence of the processing parameters, we use the same processing flow and processing parameters. Figs. 10, 11, 12, and 13 compare the time slices of the Kirchhoff prestack time migration at 300, 500, 1000, and 2000 ms, respectively, in Schemes VII and VIII. From these results, images from Scheme VIII are more severely contaminated by the footprint than those of Scheme VII, to the extent that the small complex faults cannot be easily identified. Of all the time slices, the slices at 2000 ms are least influenced by the footprint for both schemes. However, the slice of Scheme VIII at 2000 ms seems to be contaminated by more noise than that of Scheme VII, which could be due to the fact that the BSC number of Scheme VIII is much larger than that of Scheme VII.

CONCLUSIONS

Seismic acquisition footprints are non-uniform amplitude distributions among bins that vary with offsets and azimuths. In this article, we presented a quantitative calculation of acquisition footprints for 3D seismic acquisition geometries at an any target depth. The calculation is based on the WRW model,

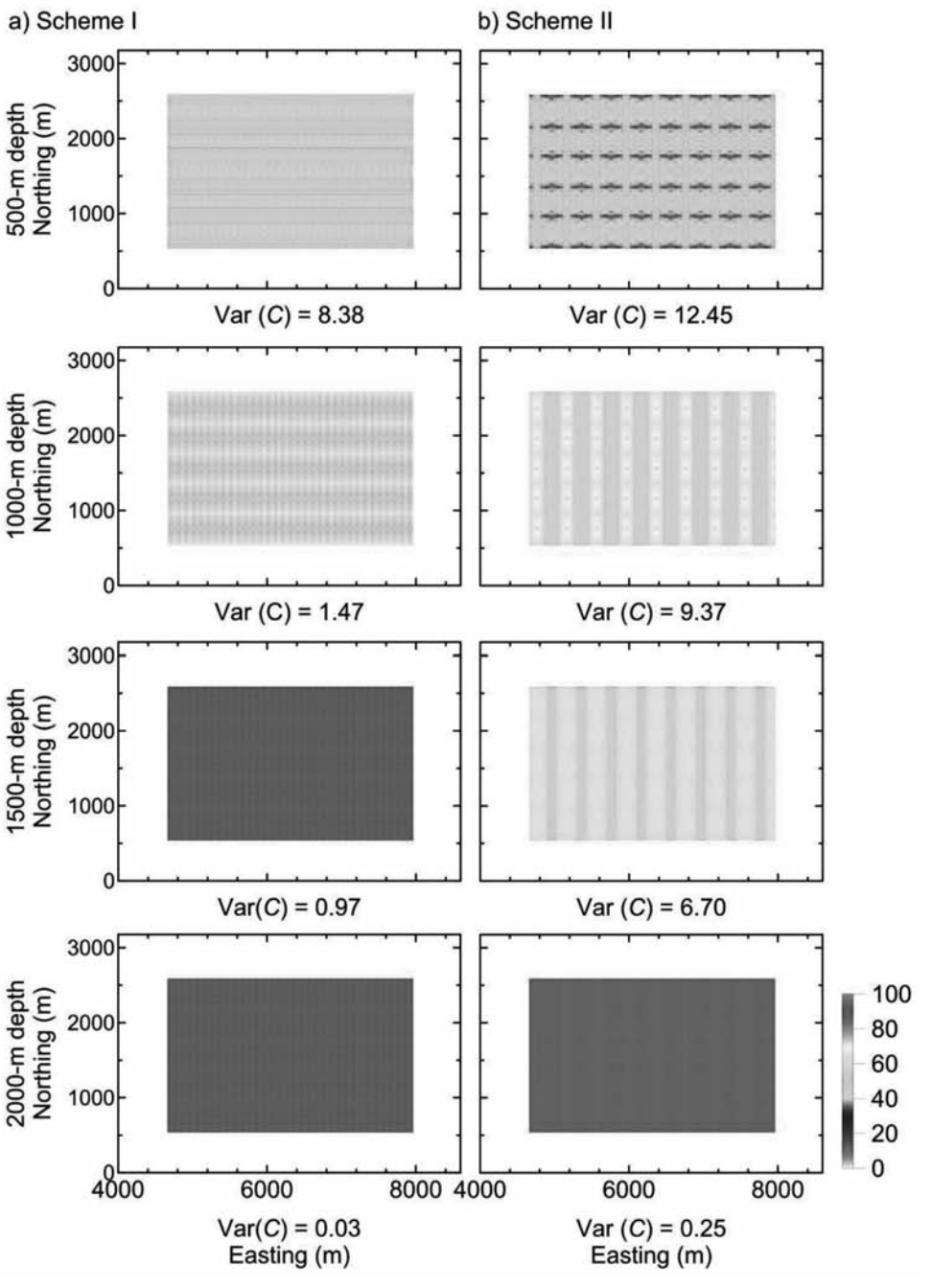

Fig. 9. Footprint distributions for acquisition Scheme VII (a) and VIII (b) (Table 3) at depth of 500 m, 1000 m, 1500 m and 2000 m, respectively.

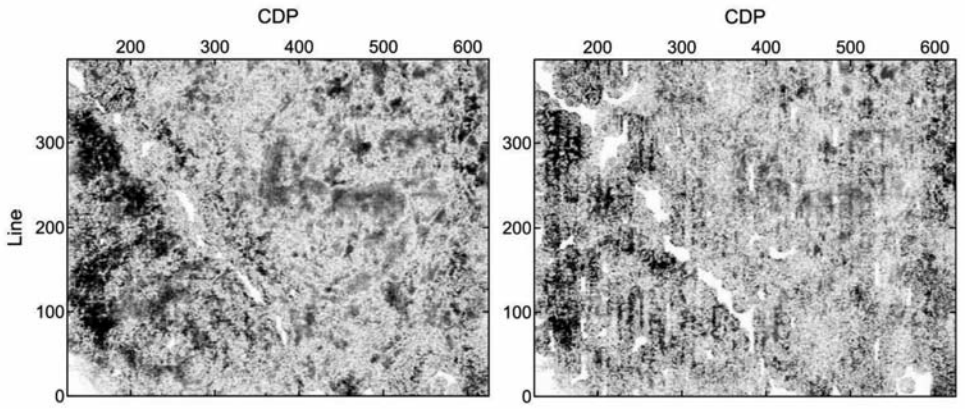

Fig. 10. The time slice at 300 ms of Kirchhoff prestack time migration for Scheme VII (left) and VIII (right).

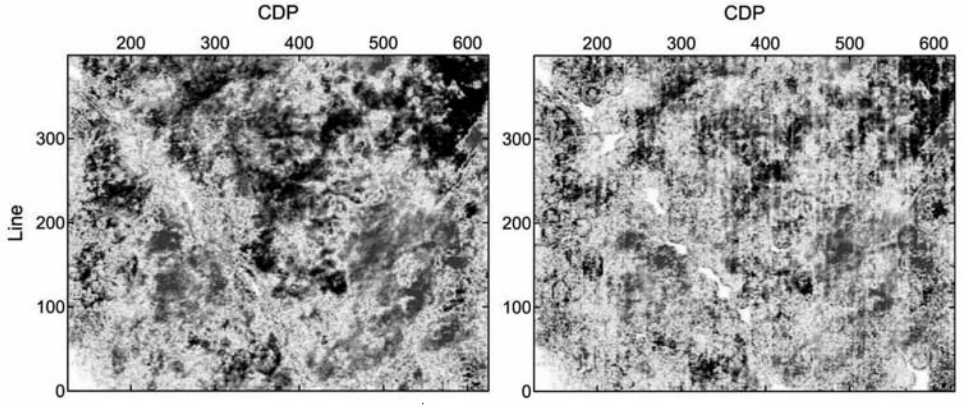

Fig. 11. The time slice at 500 ms of Kirchhoff prestack time migration for Scheme VII (left) and VIII (right).

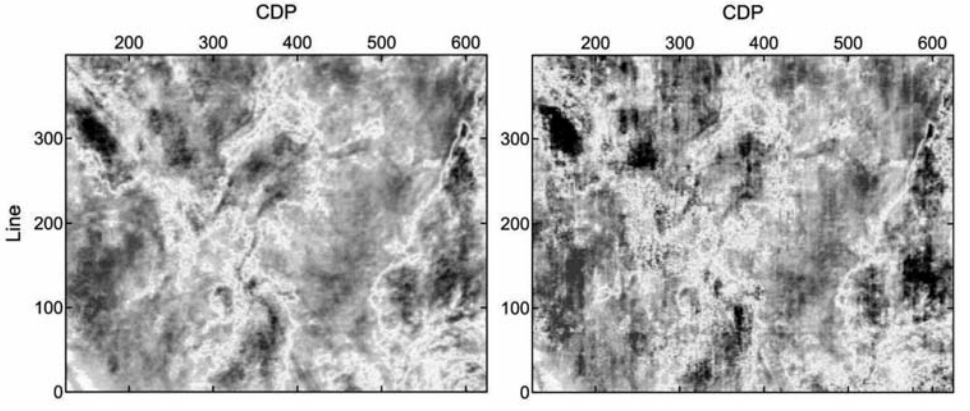

Fig. 12. The time slice at 1000 ms of Kirchhoff prestack time migration for Scheme VII (left) and VIII (right).

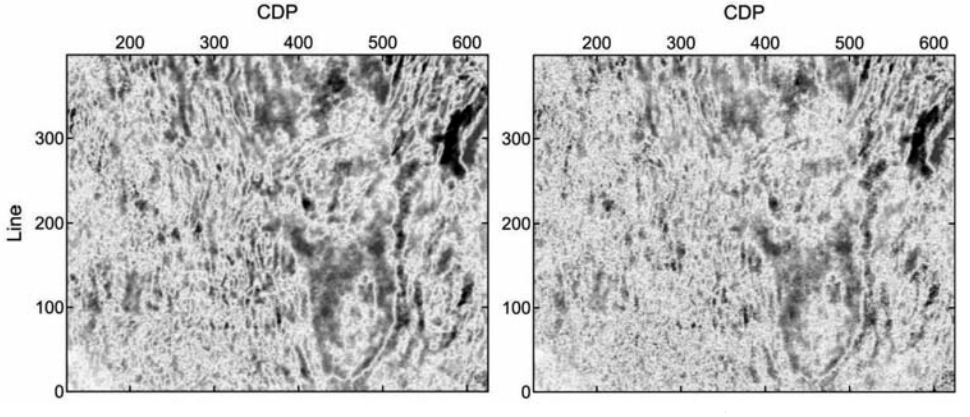

Fig. 13. The time slice at 2000 ms of Kirchhoff prestack time migration for Scheme VII (left) and VIII (right).

resulting in a stack response of primaries for every source-receiver pair. The footprint distributions of several acquisition geometries with different inline/crossline rolling distances were examined. The results of two theoretical examples indicate that the both the shot traverse spacing (S and the number of receiver lines to be repeated in the crossline roll-along K have a significant impact on the spatial uniformity of footprint distributions. We also applied the proposed method to compare two real acquisition geometries for 3D land seismic acquisition in an oilfield in China. The results of the acquisition footprints in the final migration images are in accordance with our method of theoretical footprint analysis at different target depths. Both theoretical examples and the practical case study suggest that the proposed footprint calculation can be applied to design 3D seismic surveys. The optimal acquisition geometry with the smallest possible footprint would be picked before initiating fieldwork with the proposed approach. Further, the quality of the raw seismic datasets and the final migration images would be improved with this method.

ACKNOWLEDGMENTS

We are grateful to anonymous reviewers for the constructive review and help in editing the original manuscript. The research was supported by the Natural Science Foundation of China (Grant Nos. 41204098, 41130418 and 41474105) and the National High Technology Research and Development Program (863 Program) of China (Grant No. 2013AA064202). The support from the National Science and Technology Major Project (Grant No. 2011ZX05023-005-004) are also appreciated.

REFERENCES

Al-Bannagi, M.S., Fang, K., Kelamis, P.G. and Douglass, G.S., 2005. Acquisition footprint suppression via the truncated SVD technique: Case studies from Saudi Arabia. The Leading Edge, 24: 832-834.

Berkhout, A.J., 1982. Seismic Migration, Imaging of Acoustic Energy by Wavefield Extrapolation. A: Theoretical Aspects. Elsevier Science Publishers, Amsterdam.

Berkhout, A.J., 1987. Applied Seismic Wave Theory. Advances in Exploration Geophysics. Elsevier Science Publishers, Amsterdam.

Berkhout, A.J., 1997. Pushing the limits of seismic imaging, Part I: Prestack migration in terms of double dynamic focusing. Geophysics, 62: 937-953.

Berkhout, A.J., OngKiehong, L., Volker, A.W.F. and Blacquière, G, 2001. Comprehensive assessment of seismic acquisition geometry by focal beams-Part I: Theoretical considerations. Geophysics, 66: 911-917.

Brown, R.J., 2010. Acquisition footprints and seafloor coupling in multicomponent OBC seismic data. Geophysics, 75: Q11-Q20.

Canning, A. and Gardner, G.H., 1998. Reducing 3-D acquisition footprint for 3-D DMO and 3-D prestack migration. Geophysics, 63: 1177.

Cooper, J.K., Margrave, G.F. and Lawton, D.C., 2008. Numerical modeling of seismic acquisition footprint. Expanded Abstr., 78th Ann. Internat. SEG Mtg., Las Vegas: 25-29.

Cordsen, A., 2004. Acquisition footprint can confuse. AAPG Explorer, March 2004: 26.
Di, B., Xu, X. and Wei, J., 2008. Wide/narrow azimuth acquisition footprints and their effects on seismic imaging. Petrol. Sci., 5: 308-313.
Gesbert, S., 2002. From acquisition footprints to true amplitude. Geophysics, 67: 830-839.
Hill, S., Shultz, M. and Brewer, J., 1999. Acquisition footprint and fold-of-stack plots. The Leading Edge, 18: 686-695.
Marfurt, K.J., Scheet, R.M., Sharp, J.A. and Harper, M.G., 1998. Suppression of the acquisition footprint for seismic sequence attribute mapping. Geophysics, 63: 1024-1035.
Marschall, R., 1997. 3D Acquisition of Seismic Data. Vol. 17, DGMK-Mintrop-Seminar, Perspektiven in Akquisition und Processing seismischer Daten, Münster: 27-84. DGMK und Unikontakt Ruhr-Universität Bochum.
Marschall, R., 1999. 4D seismics - principles and applications. J. Seismic Explor., 8: 309-346.
Marschall, R., 2003. 4D Seismics: 7th Internat. Forum Reservoir Simulat., June 23-27, Schlosshotel Bühlerhöhe, Germany.
Mallick, S. 1993, A simple approximation to the P-wave reflection coefficient and its implication in the inversion of amplitude variation with offset data. Geophysics, 58: 544-552.
Officer, C.B., 1958. Introduction to the Theory of Sound Transmission. McGraw Hill Book Co., New York.
Savage, J.E.G. and Mathewson, J.C., 2001. Prediction of 3-D seismic footprint from existing 2-D data. The Leading Edge, 20: 464-473.
Schuster, G.T., Liu, Z., 2001. Seismic array theorem and rapid calculation of acquisition footprint noise. Geophysics, 66: 1843-1849.
Volker, A.W.F., Blacquière, G., Berkhout, A.J. and OngKiehong, L., 2001. Comprehensive assessment of seismic acquisition geometries by focal beams - Part II: Practical aspects and examples. Geophysics, 66: 918-931.
Van Veldhuizen, E.J., Blacquière, G. and Berkhout, A.J., 2008, Acquisition geometry analysis in complex 3D media. Geophysics, 73: Q43-Q58.
Vermeer, G.J.O., 1997. Streamers versus stationary receivers. OTC Proc.: 331-346.
Vermeer, G.J.O., 1998. 3-D symmetric sampling. Geophysics, 63: 1629-1647.
Vermeer, G.J.O., 2012. 3-D Seismic Survey Design. SEG, Tulsa, OK.
Wei, W., Fu, L.Y. and Blacquière, G., 2012. Fast multifrequency focal beam analysis for 3D seismic acquisition geometry. Geophysics, 77: P11-P21.